ORIGINAL PAPER

Dynamics and stability of flow down a flexible incline

Omar K. Matar · Satish Kumar

Abstract   The flow of a thin liquid film down a flexible inclined wall is examined. Two configurations are studied: constant flux (CF) and constant volume (CV). The former configuration involves constant feeding of the film from an infinite reservoir of liquid. The latter involves the spreading of a drop of constant volume down the wall. Lubrication theory is used to derive a pair of coupled two-dimensional nonlinear evolution equations for the film thickness and wall deflection. The contact-line singularity is relieved by assuming that the underlying wall is pre-wetted with a precursor layer of uniform thickness. Solution of the one-dimensional evolution equations demonstrates the existence of travelling-wave solutions in the CF case and self-similar solutions in the CV case. The effect of varying the wall tension and damping coefficient on the structure of these solutions is elucidated. The linear stability of the flow to transverse perturbations is also examined in the CF case only. The results indicate that the flow, which is already unstable in the rigid-wall limit, is further destabilized as a result of the coupling between the fluid and underlying flexible wall.

Keywords   Thin film · Flexible · Lubrication · Stability

1 Introduction

The spreading of thin liquid films on solid substrates has been well studied in the literature due to its importance to numerous industrial and daily-life settings [1–5]. These films are driven to spread either by body (e.g., gravity) or surface (e.g., Marangoni) forces. A system which has received particular attention is that of gravity-driven flow of a thin film down an inclined plane, due to its applicability in coating-flow technology. Numerous experimental and modeling studies have demonstrated that this flow is susceptible to fingering instabilities. During the course of the flow, the film develops a thick capillary ridge near the

O. K. Matar (✉)
Department of Chemical Engineering, Imperial College London, South Kensington Campus, London, SW7 2AZ, UK
e-mail: o.matar@imperial.ac.uk

S. Kumar
Department of Chemical Engineering and Materials Science, University of Minnesota, 151 Amundson Hall,
421 Washington Ave. SE, Minneapolis, MN 55455, USA
e-mail: kumar@cems.umn.edu

contact-line region which becomes linearly unstable to transverse perturbations of intermediate wave-numbers. These perturbations grow to give rise to fingers in the nonlinear regime. The mechanism for the instability has been shown to be due to the applied body force (whether gravitational or centrifugal in nature) [6], which causes thicker regions of the ridge to travel faster than relatively thin regions. Streamwise capillarity provides the high wave number cut-off for the instability.

In contrast to flow down a rigid inclined plane, the problem of flow down a *flexible* inclined plane has not, to our knowledge, received attention in the literature. As flow down a rigid incline is unstable, it is of interest to determine ways in which such a flow can be stabilized. One potential way to do this is to make the incline flexible. The flowing fluid will exert forces on the flexible incline, which may then deform. This deformation will affect the fluid flow, and possibly its stability to various disturbances. Similar elastohy-drodynamic problems arise in the use of flexible boundaries to delay the transition to turbulence [7], the modeling of airflow in pulmonary airways [8] and hemodynamics in the heart [9], the reduction of defects in coating process via the use of rubber-covered rolls [10], and instabilities near polymer interfaces [11]. Recently, Matar and Kumar [12] examined the rupture of a surfactant-covered thin film on a flexible wall and found that the properties of the substrate (tension and damping, for instance) can have a significant effect on the rupture dynamics. From a practical point of view, studying the flow down a flexible incline may be relevant to coating processes in which fluids flow down inclined planes or coat flexible substrates.

As a model system in the present work, we consider the dynamics and stability of a thin liquid film flowing down a flexible wall. We use lubrication theory to derive a pair of coupled evolution equations for the wall deflection and film height. The flow in the absence of disturbances (base state) is investigated for different values of the damping coefficient and wall tension. Two different flow configurations are examined: constant flux and constant volume. The first corresponds to the case in which a constant flux of liquid is provided at the flow origin, while the second involves the spreading of a drop of finite volume. The existence of travelling-wave solutions in the former case is demonstrated and the effect of wall tension and damping on the linear stability of the system in this case is then examined. Our results indicate that decreasing the relative significance of wall damping and/or wall tension is destabilizing, leading to an increase in the maximal growth rates and band of unstable wavenumbers. In the limit of large wall tensions, the situation of flow over a rigid wall is recovered.

2 Formulation

The liquid film is assumed to be incompressible, Newtonian and uncontaminated with characteristic thickness H, length L, viscosity μ, density ρ and surface tension σ. The flexible wall, which is inclined at an angle θ to the horizontal, has thickness H_0, density ρ_w, tension T and damping coefficient γ. The contact-line singularity is relieved by using a precursor film of thickness H_b. We use a rectangular coordinate system (x, y, z) to describe the flow and a velocity field $\mathbf{u} = (u, v, w)$, where u, v and w correspond to the streamwise, transverse and vertical components of the velocity, respectively. The instantaneous location of the film height is at $z = h(x, y, t)$, while that of the underlying flexible wall is at $z = -\eta(x, y, t)$. The dynamics of the surrounding air, which has pressure p_g, are neglected in the present work.

The film dynamics are governed by mass and momentum conservation equations in $-\eta \leq z \leq h$:

$$\nabla \cdot \mathbf{u} = 0, \quad \rho \frac{D\mathbf{u}}{Dt} = -\nabla p + \mu \nabla^2 \mathbf{u} + \rho \mathbf{g}, \tag{1}$$

in which p and $\mathbf{g}$ denote the pressure and the gravity vector, respectively. The following boundary conditions apply at $z = h(x, y, t)$:

$$\mathbf{n} \cdot \mathbf{T} \cdot \mathbf{n} = \sigma \kappa, \quad \mathbf{n} \cdot \mathbf{T} \cdot \mathbf{t} = 0, \quad h_t + u_s h_x + v_s h_y = w_s, \tag{2}$$

where $\kappa = \nabla_s \cdot \mathbf{n}$, $\nabla_s = (\mathbf{I} - \mathbf{nn}) \cdot \nabla$, $\mathbf{T} = -p\mathbf{I} + \mu(\nabla \mathbf{u} + \nabla \mathbf{u}^T)$ and the subscript 's' denotes surface quantities; unless stated otherwise, subscripts denote partial differentiation. These conditions correspond

to the continuity of shear and normal stress and the kinematic boundary condition, respectively. Here, $\mathbf{T}$ is the total stress tensor in the liquid film, κ is the curvature, $\mathbf{n} = (-h_x, -h_y, 1)/(1 + h_x^2 + h_y^2)^{1/2}$ is the outward pointing normal from the air–liquid interface, $\mathbf{t}$ is the tangent to the air–liquid interface and $\mathbf{I}$ is the identity tensor.

The conditions at $z = -\eta$ are:

$$u = v = 0, \quad \eta_t = -w_\text{w}, \tag{3}$$

which correspond to the no-slip and no-penetration conditions, and the kinematic boundary condition, respectively; the subscript 'w' designates quantities evaluated at the flexible wall.

For the wall, we have the following governing equation:

$$\left(\frac{\rho_\text{w} H_0 \gamma}{\Delta_w}\right) \eta_t - \left(\frac{T}{\Delta_\text{w}^3}\right) (\eta_{xx} + \eta_{yy}) = -\mathbf{n}_\text{w} \cdot \mathbf{T} \cdot \mathbf{n}_\text{w}, \tag{4}$$

in which $\mathbf{n}_\text{w} = (-\eta_x, -\eta_y, 1)/\Delta_\text{w}$ is the unit normal to the wall–liquid interface where $\Delta_\text{w} \equiv (1 + \eta_x^2 + \eta_y^2)^{1/2}$. This model is similar to that used by Halpern and Grotberg [13, 14] in their work on liquid-film dynamics inside flexible tubes, and by Matar and Kumar [12] in their study of thin-film rupture on flexible walls. The wall is assumed to be infinitely long, isotropic, impermeable and sufficiently thin so that wall tension (assumed to be the same in the longitudinal and transverse directions) acts uniformly across the wall thickness. Bending stresses are neglected under these conditions [15, 16].

The above equations are rendered dimensionless by scaling x and y on L, z, h and η on H, u and v on U, w on ϵU, t on L/U and p on $\rho g L$ where $g = |\mathbf{g}|$. Here, $U = \rho g H^2/\mu$ is a characteristic velocity, $L = (\sigma H/\rho g)^{1/3}$ is the characteristic length and $\epsilon \equiv H/L$. Assuming that $\epsilon \ll 1$, we can employ lubrication theory, which to leading order gives:

$$h_t = -\eta_t + \frac{1}{3}\left[(h + \eta)^3(p_x - \sin\theta)\right]_x + \frac{1}{3}\left[(h + \eta)^3 p_y\right]_y, \tag{5}$$

$$\epsilon^2 \mathcal{B} \eta_t - \mathcal{T}(\eta_{xx} + \eta_{yy}) = -(h_{xx} + h_{yy}), \tag{6}$$

where $p = -(h_{xx} + h_{yy})$. Here, $\mathcal{B} \equiv \rho_\text{w} H_0 H \gamma/\mu$ and $\mathcal{T} \equiv T/\sigma$, which are dimensionless measures of wall damping and tension, respectively. In what follows, we shall set $\mathcal{B} = B/\epsilon^2$ (except where we analyze the early time dynamics) but explore a wide range of B values. Note that as $\eta \to 0$ (either because $\mathcal{T} \to \infty$ and/or $\mathcal{B} \to \infty$), Equation 5 reduces to that governing the two-dimensional dynamics of a thin film flowing down a rigid incline.

Solutions of Eqs. 5 and 6 will be obtained for two distinct situations: the case of a constant volume (CV) of fluid and that of constant flux (CF). The former case represents a situation in which a drop of liquid of finite volume spreads along the flexible incline. The latter represents flow of a thin sheet of liquid down the incline which emerges from a reservoir of liquid. In the CV case, numerical solutions of the one-dimensional (1-D) version of Eqs. 5 and 6 are sought starting from:

$$h(x, 0) = \exp(-(x - 20)^2) + b, \quad \eta(x, 0) = 0, \tag{7}$$

which correspond to a liquid drop deposited on a substrate with zero deflection, where b is the dimensionless precursor-film thickness. The boundary conditions are:

$$\begin{aligned} h_x(0, t) = h_{xxx}(0, t) = 0, \quad &\eta(0, t) = 0, \\ h(\mathcal{L}, t) = b, \quad h_x(\mathcal{L}, t) = 0, \quad &\eta(\mathcal{L}, t) = 0, \end{aligned} \tag{8}$$

where $\mathcal{L}$ is the length of the computational domain. In the CF case, Eqs. 5 and 6 admit travelling-wave solutions of the form:

$$h(x, t) = H(\xi), \quad \eta(x, t) = G(\xi), \tag{9}$$

where $\xi = x - ct$ in which c is the travelling-wave velocity. The coupled system of ordinary differential equations governing $H(\xi)$ and $G(\xi)$ is then given by

$$\left[c(G + H) - \frac{1}{3} \left[(H + G)^3 \left(H_{\xi\xi\xi} + \sin\theta \right) \right] \right]_\xi = 0, \tag{10}$$

$$\left[\mathcal{T} G_\xi - H_\xi + cBG \right]_\xi = 0. \tag{11}$$

An expression for c is obtained via integration of Eq. 10 and application of the conditions $H \rightarrow b$ and $H_{\xi\xi\xi} \rightarrow 0$ as $\xi \rightarrow \infty$, and $H \rightarrow 1$ and $H_{\xi\xi\xi} \rightarrow 0$ as $\xi \rightarrow -\infty$:

$$c = \frac{(1 - b^3)}{3(1 - b)} \sin\theta, \tag{12}$$

which is dependent on b and θ only and independent of both $\mathcal{T}$ and B. This expression for c is identical to that for flow over a rigid incline [6, 17].

Rather than solve the ordinary differential equations given by Eqs. 10 and 11, travelling-wave solutions are constructed by assuming that $h(x, t) = H(\xi, \tau)$, $\eta(x, t) = G(\xi, \tau)$, $\tau = t$ and seeking steady-state solutions of Eqs. 10 and 11 starting from the following initial conditions:

$$H(\xi, 0) = 0.5(1 - b) \left(1 - \tanh \left(10 \left[\xi - 10 \right] \right) \right) + b, \quad \eta(\xi, 0) = 0, \tag{13}$$

and with the following boundary conditions:

$$\begin{aligned} H(0, \tau) = 1, \quad H_\xi(0, \tau) = 0, \quad G(0, \tau) = 0, \\ H(\mathcal{L}, \tau) = b, \quad H_\xi(\mathcal{L}, \tau) = 0, \quad G(\mathcal{L}, \tau) = 0. \end{aligned} \tag{14}$$

The initial condition for the film thickness corresponds to a film whose thickness changes from 1 to b over 10 dimensionless units. Note that the use of other forms for the initial conditions in both the CV and CF cases gives rise to quantitative, rather than qualitative variations in the results.

The numerical procedure used to carry out the computations is PDECOL, in which finite elements are used to discretize the spatial derivatives; Gear's method is employed in order to advance the solution in time. This routine has been previously used to solve thin-film equations in related problems [18, 19] where the film exhibits spatially rapidly varying solutions in the form of advancing fronts and pulses, and thickened capillary ridges. Numerical solutions for the CV case were obtained over a computational domain of length up to 200 dimensionless units using up to 3000 grid points; convergence was achieved upon refinement of the spatial mesh size. These solutions were obtained for $0.01 \leq \mathcal{T} \leq 100$ and $10^{-6} \leq B \leq 100$. In the CF case, travelling-wave solutions were obtained for $0.01 \leq \mathcal{T} \leq 10$ and $10^{-6} \leq B \leq 100$ over a computational domain of length 20 dimensionless units. In this case, up to 600 grid points were used with convergence again being achieved upon mesh refinement. For both configurations, θ and ϵ were fixed at $\pi/2$ and 0.01, respectively. The parameter b was fixed at 0.1 and 0.04 for the CF and CV cases, respectively.

3 Base flow

3.1 Constant flux

We begin by examining the solutions obtained for the case of weak tension and damping at early times. Setting $\mathcal{T} = \epsilon \hat{\mathcal{T}}$ and $t = \epsilon^2 \hat{t}$ with $\mathcal{B} = \mathrm{O}(1)$ Eqs. 5 and 6 can be expressed as:

$$\mathcal{B}\eta_{\hat{t}} = -h_{xx} + \mathrm{O}(\epsilon^2), \quad h_{\hat{t}} = -\eta_{\hat{t}} + \mathrm{O}(\epsilon^2). \tag{15}$$

Thus, h obeys a diffusion equation:

$$h_{\hat{t}} = \mathcal{B}^{-1} h_{xx}, \tag{16}$$

with $\mathcal{B}^{-1}$ as the effective diffusion coefficient. Equation 16 admits the following analytical solution:

$$h(x,\hat{t}) = \frac{1}{2}\left[(1+b) - (1-b)\mathrm{erf}\left(\frac{(x-x_0)}{2\sqrt{\hat{t}/\mathcal{B}}}\right)\right], \tag{17}$$

which satisfies the boundary conditions $h = 1$ at $x = 0$ and $h \to b$ as $x \to \infty$. An early-time solution for η can also be obtained from Eq. 15, which takes into account the initial conditions given by (13):

$$\eta(x,\hat{t}) = \frac{1}{2}(1-b)\left(1 - \tanh\left(10\left[x - x_0\right]\right)\right) + b - \frac{1}{2}\left[(1+b) - (1-b)\mathrm{erf}\left(\frac{x}{2\sqrt{\hat{t}/\mathcal{B}}}\right)\right]. \tag{18}$$

Figure 1a, b depicts a comparison between numerically generated solutions of h and η at early times, starting from Eq. 13, with analytical solutions described by Eqs. 17 and 18. Here, $\hat{\mathcal{T}} = 0.01$, $\mathcal{B} = 1$, $\epsilon = 10^{-2}$ and $x_0 = 10$, with $t = 0$–10^{-4} (or $\hat{t} = 0$ to $\hat{t} = 1$). Inspection of Fig. 1a, b reveals excellent agreement between the analytical solutions and the numerical predictions. Also, as shown in Fig. 1a, b, the initially localized h distribution appears to relax 'diffusively' on a fast time-scale, while η, which is zero-valued initially, rapidly achieves magnitudes which are of order one. This reflects the rapid deformation of a weakly tensile wall in response to the deposition of a localized film upon it.

Next, we examine the behavior of h and η at intermediate times. As shown in Fig. 1c, d, which depicts the solutions for h and η up to $t = 0.01$, the film thickness assumes an essentially linear profile that satisfies $h = 1$ and $h = b$ at both ends of the computational domain. Close inspection of Fig. 1c, however, reveals the existence of a region of rapid variation near $x = x_0 = 10$, an 'inner' region in which the solution upstream
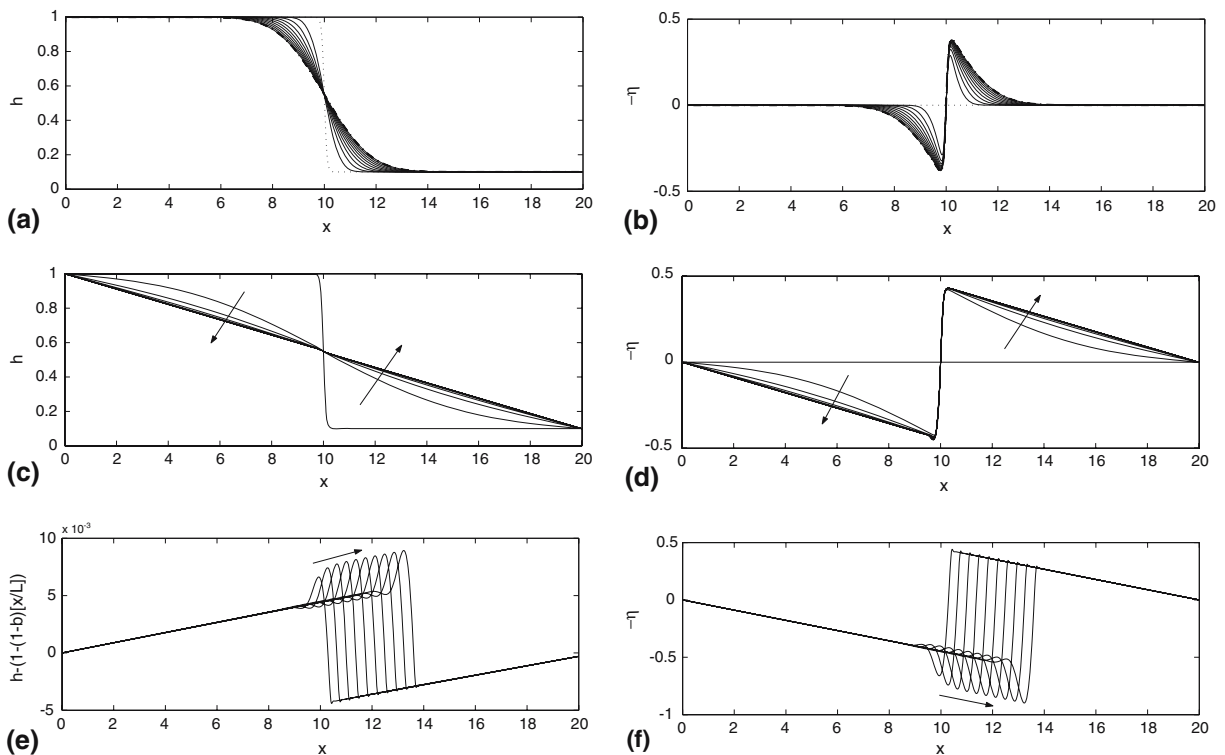

Fig. 1 Early-time evolution of the film thickness, (**a**), and substrate deflection, (**b**), for $\mathcal{T} = 0.01$ and $\mathcal{B} = 1$ with $t = 0 - 10^{-4}$ in 10 equal time steps. Both numerically generated solutions (solid lines), starting from (13) (dotted lines), and analytical solutions at $t = 10^{-4}$ (dot-dashed lines), given by Eqs. 17 and 18, are shown; (**c**) and (**d**) show the evolution at intermediate times with $t = 0 - t = 10^{-2}$ in 10 equal time steps; (**e**) and (**f**) show the evolution for $t = 0 - t = 10$ in 10 equal time steps. The arrows indicate the direction of increasing time

of x_0 adjusts onto that downstream, i.e., in the 'outer' regions. The profile for η, shown in Fig. 1d, also comprises two essentially linear portions upstream and downstream of $x = x_0 = 10$, which satisfy $\eta = 0$ at $x = (0, \mathcal{L})$. In the vicinity of $x = x_0$, a region of rapid adjustment in η is found which coincides with the spatial location of that found in Fig. 1c. The amplitude of these regions in h (η) increases with increasing (decreasing) $\mathcal{T}$.

We now examine the evolution at later times. In Fig. 1e, f, we plot the spatial development of $h - (1 - (1 - b)[x/\mathcal{L}])$ and η for $t = 0$ up to $t = 10$; here, we have subtracted the linear part of the film from the solution for h in order to present a magnified view of the capillary ridge, which has a small amplitude for relatively small $\mathcal{T}$. The film thickness and deflection profiles appear to develop thickened ridges in the adjustment region, which travel downstream of the flow origin and undergo only very minor changes in shape. At this stage, it is possible to infer from Fig. 1e, f that the solutions for h and η have become travelling-waves that move in the direction of increasing x with a constant speed, c. The emergence of these travelling-wave solutions was anticipated in the previous section.

In Fig. 2a, b, we show the effect of varying the parameter $\mathcal{T}$ on the shapes of the travelling-wave solutions with $B = 10^{-4}$ ($\mathcal{B} = 1$); these solutions are, of course, steady in a reference frame moving with the wave. Also shown in Fig. 2a, b are the profiles associated with flow over a rigid wall, obtained by setting $\mathcal{T} \to \infty$. Clearly, an increase in the value of the axial tension leads to an overall reduction in the amplitude of the wall deflection and increase in that of the capillary ridge developed by the film thickness; the profiles associated with $\mathcal{T} = 10$ are very similar to those generated with $\mathcal{T} \to \infty$. In the case of weak tension, pronounced ridges are exhibited by G reflecting the large deformations in the wall which accompany the flow in this case.

This behavior, which is to be expected intuitively, can also be rationalized by examining Eqs. 5 and 6 in the absence of wall damping, i.e., for $B \ll 1$. In this case, Eq. 6 reduces to:

$$\eta_{xx} = h_{xx}/\mathcal{T}, \tag{19}$$

whence $\eta = h/\mathcal{T} + c_1(t)x + c_2(t)$, where c_1 and c_2 are constants of integration. Application of the boundary conditions appropriate to the CF case yields the following expression for η:

$$\eta = \frac{[h + (1 - b)x/\mathcal{L} - 1]}{\mathcal{T}}, \tag{20}$$

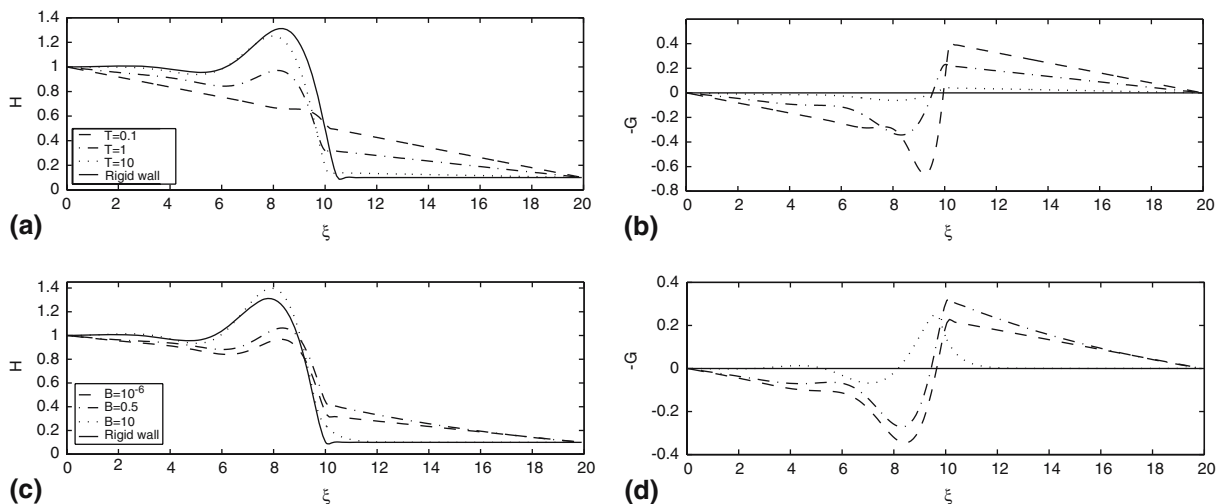which suggests that the amplitude of η decreases with increasing $\mathcal{T}$ (and vice versa).

Fig. 2 The effect of $\mathcal{T}$ (with $B = 10^{-4}$), (**a**) and (**b**), and B (with $\mathcal{T} = 1$), (**c**) and (**d**), on H and G

We next examine the effect of varying B on the structure of the travelling-wave solutions. As shown in Fig. 2c, d, in which we vary B over seven orders of magnitude while keeping $\mathcal{T} = 1$, decreasing B (i.e., decreasing the relative significance of wall damping) results in smaller film capillary ridges and more pronounced deformations in the underlying wall. In contrast, increasing B to large values yields profiles that are very similar to those associated with flow over a rigid wall, which are also shown in Fig. 2c, d. Interestingly, the profiles associated with $B = 10$ and $\mathcal{T} = 1$ exhibit capillary ridges which are more pronounced than those found in the rigid-wall case. A further increase in B for fixed $\mathcal{T}$ values, however, yields profiles which are virtually identical to those associated with a rigid wall.

3.2 Constant volume

We begin this section by examining the flow profiles associated with the spreading of a drop of constant volume down a rigid incline. In Fig. 3a, we plot the evolution of h and the temporal variation of the maximal value of h, h_{max}, and that of its spatial location, x_{max}, in panels (b) and (c), respectively. Inspection of Fig. 3a reveals that the liquid drop has undergone significant deformation and spreads asymmetrically under the action of gravity down the inclined plane. The drop develops a thickened capillary ridge at its leading edge, which is very similar to that seen in Fig. 1e in the CF case. Inspection of Figs. 3b and c shows that both h_{max} and x_{max} follow different scalings at different stages of the flow. Specifically, $h_{max} \sim t^{-1/7}$ and $x_{max} \sim t^{1/7}$, and $h_{max} \sim t^{-1/3}$ and $x_{max} \sim t^{1/3}$ [1, 20], at early and late times, respectively. We shall return to this issue later in this section where arguments will be provided for the determination of these scaling exponents.
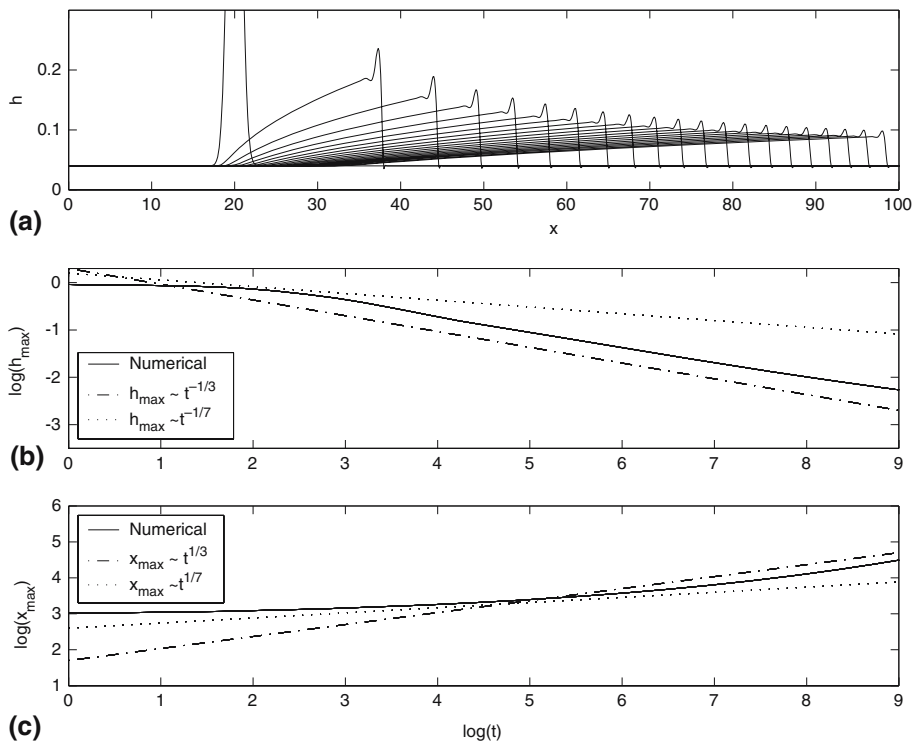

Fig. 3 Evolution of the drop thickness, (**a**), and the temporal evolution of the maximal thickness h_{max}, (**b**), and of the spatial location of h_{max}, x_{max}, (**c**), for a rigid incline. The times shown in panels (**a**) and (**b**) correspond to $t = 0$–10000 in 20 equal steps
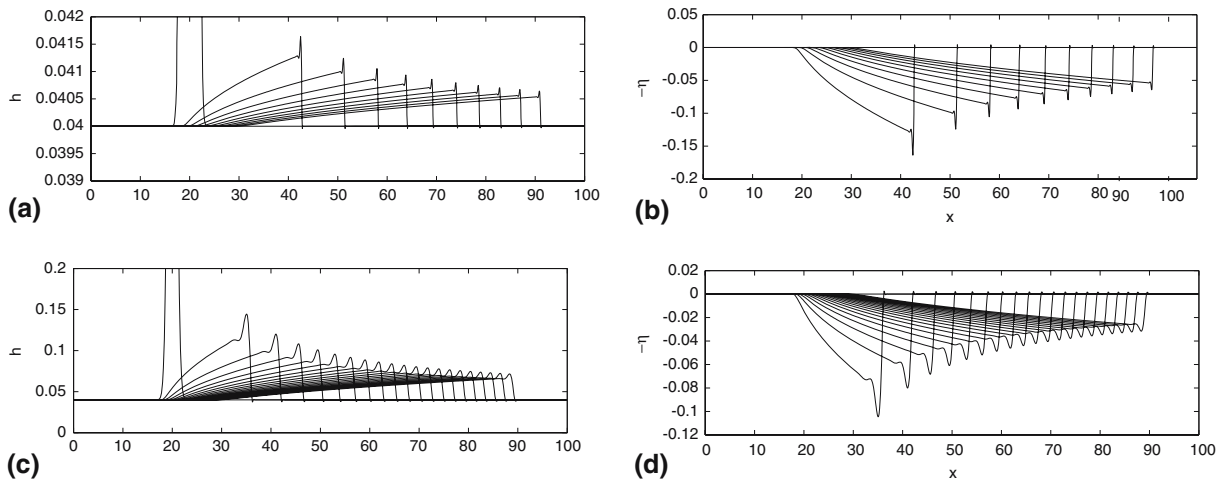
Fig. 4 Evolution of the drop thickness and substrate deflection. (**a**) and (**b**): $\mathcal{T} = 0.01$ and $B = 10^{-6}$; (**c**) and (**d**): $\mathcal{T} = 1$ and $B = 10^{-6}$. The times shown correspond to $t = 0$–8100 in 20 equal steps

In Fig. 4a, b, we show the evolution of h and η for the case of weak tension and damping, characterized by $\mathcal{T} = 0.01$ and $B = 10^{-6}$. Inspection of Fig. 4a reveals that the amplitude of the capillary ridge exhibited by the deformed drop is small in this case. The η profiles also exhibit 'ridges' that coincide with those in h, which, however, are of larger amplitudes as expected for small $\mathcal{T}$ and B. In fact, from Eq. 19, which is valid for negligible wall damping, it can be shown that in the CV case

$$\eta = \frac{h-b}{\mathcal{T}}, \tag{21}$$

which suggests that the amplitude of η is inversely proportional to the magnitude of $\mathcal{T}$. The profiles for both h and η exhibit 'outer' and 'inner' regions, similar to those observed in the rigid-wall case [17, 20]. In the outer region, the flow is dominated by gravity, viscosity and wall characteristics, while in the inner region, capillarity is also significant.

We next investigate the effect of varying $\mathcal{T}$ and B on the evolution of h and η. Our results suggest that increasing $\mathcal{T}$ while keeping B constant leads to a reduction in the degree of deformation of the flexible wall and an increase in the amplitude of the fluid capillary ridges. An increase in $\mathcal{T}$ also results in smoother profiles in both h and η, characterized by wider, less pulse-like ridges, as shown in Fig. 4c, d. We have also found that increasing B by two orders of magnitude from the value used in Fig. 4a, b while keeping $\mathcal{T} = 0.01$ constant appears to have a minor effect on the shapes of the profiles for h and η (not shown). This is due to the fact that the wall damping term in Eq. 6 contains a ϵ^2 pre-factor. Thus, in order for these effects to be significant, B must be increased such that $B \sim O(1)$.

We have also investigated the effect of varying $\mathcal{T}$ and B on the scaling exponents at early and late times. In Fig. 5a, b, we plot the temporal evolution of $(\eta + h)_{\max}$ and that of its spatial location, $x_{\max}$, for the same parameters as those used to generate Fig. 4a, b. Clearly, $(\eta + h)_{\max}$ and $x_{\max}$ follow similar scalings to those observed in Fig. 3 for the case of a rigid wall at both early and late times. It therefore appears that the scaling exponents—which in the rigid-wall case (as will be shown below) are solely determined by balancing gravity, capillarity and viscous retardation—persist despite the presence of a highly compliant wall. In fact, increasing $\mathcal{T}$ (and $\mathcal{B}$, not shown) also appears to have no discernible effect on these exponents (see Fig. 5c, d).

In order to explain the scaling behavior exhibited by h and η, we seek self-similar solutions of Eqs. 5 and 6 of the following form:

$$\eta(x,t) = \mathcal{G}(\xi)t^{\beta}, \quad h(x,t) = \mathcal{H}(\xi)t^{\beta}, \quad \xi = xt^{-\alpha}, \tag{22}$$
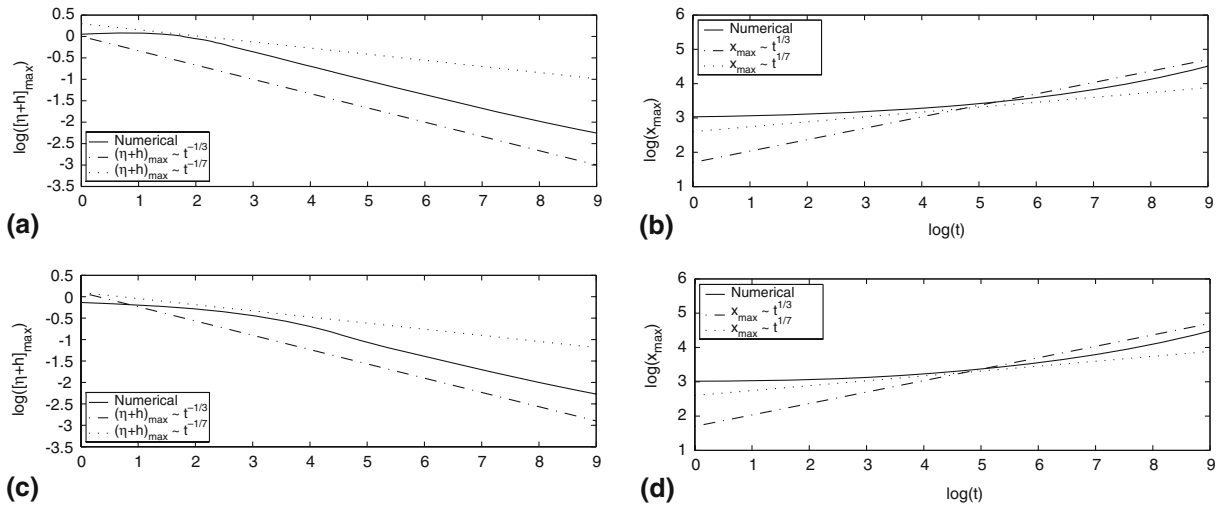
Fig. 5 Temporal evolution of the maximal values of the drop thickness and surface deflection, $(\eta + h)_{\max}$, and of the spatial location of $(\eta + h)_{\max}$ and $x_{\max}$. (**a**) and (**b**): $\mathcal{T} = 0.01$ and $B = 10^{-6}$; (**c**) and (**d**): $\mathcal{T} = 1$ and $B = 10^{-6}$. The remaining parameter values are the same as in Fig. 4

where we have implicitly assumed that η and h follow the same scalings in time. Substitution of these rescalings into Eqs. 5 and 6 yields:

$$B \left(\beta \mathcal{G} - \alpha \xi \mathcal{G}_\xi \right) = t^{1-2\alpha} \left(\mathcal{T} \mathcal{G}_{\xi\xi} - \mathcal{H}_{\xi\xi} \right), \tag{23}$$

$$\beta \left(\mathcal{H} + \mathcal{G} \right) - \alpha \xi \left(\mathcal{H} + \mathcal{G} \right)_\xi + \frac{t^{1+3\beta-4\alpha}}{3} \left[\left(\mathcal{H} + \mathcal{G} \right)^3 \left(\mathcal{H}_{\xi\xi\xi} + t^{3\alpha-\beta} \sin\theta \right) \right]_\xi = 0. \tag{24}$$

In the CV case, the volume of the drop, V, is an invariant: $V = t^{\alpha+\beta} \int_0^\infty \mathcal{H} d\xi$. Thus, in order to obtain self-similar solutions, $\beta = -\alpha$, where it is expected that $\alpha > 0$.

At this stage, it is possible to derive values of the scaling exponents which are valid at early and late times. One would expect intuitively that, at early times, a balance would exist between capillary and viscous forces due to the large initial curvature of the drop, with gravitational acceleration playing only a minor role. At later times, after which the drop had undergone considerable deformation, the dominant balance would instead be between gravitational acceleration and viscous retardation. At early times, $\mathcal{H}_{\xi\xi\xi} \gg t^{4\alpha}$, so that Eq. 24 effectively reduces to:

$$\left[\beta \xi \left(\mathcal{H} + \mathcal{G} \right) + \frac{t^{1+3\beta-4\alpha}}{3} \left(\mathcal{H} + \mathcal{G} \right)^3 \mathcal{H}_{\xi\xi\xi} \right]_\xi = 0, \tag{25}$$

suggesting that the early-time dynamics are dominated by capillarity rather than gravity. In this case, we have:

$$\alpha = \frac{1}{7} \quad \text{and} \quad \beta = -\frac{1}{7}. \tag{26}$$

Note that $t^{1-2\alpha}$ is then $t^{5/7}$. Thus, from Eq. 23, $\beta \mathcal{G} \approx \alpha \xi \mathcal{G}_\xi$ at early times, which implies that $\mathcal{G} \approx \mathcal{G}_0/\xi$. From boundedness considerations, $\mathcal{G} \approx 0$, which suggests that the dynamics are driven by the height evolution equation at early times.

At relatively late times, the gravitational term dominates, $\mathcal{H}_{\xi\xi\xi} \ll t^{4\alpha}$, so Eq. 24 effectively becomes:

$$\left[\beta \xi \left(\mathcal{H} + \mathcal{G} \right) + \frac{t^{1+2\beta-\alpha}}{3} \left(\mathcal{H} + \mathcal{G} \right)^3 \sin\theta \right]_\xi = 0, \tag{27}$$

which may be re-expressed as:

$$\left[\beta\xi\zeta + \frac{t^{1+2\beta-\alpha}}{3}\zeta^3\sin\theta\right]_\xi = 0, \tag{28}$$

where $\zeta \equiv \mathcal{H} + \mathcal{G}$, from which:

$$\alpha = \frac{1}{3} \quad \text{and} \quad \beta = -\frac{1}{3}. \tag{29}$$

This suggests that in this regime, $(\eta + h)_{\max} \sim t^{-1/3}$, and due to mass conservation, $x_{\max} \sim t^{1/3}$. In fact, an expression for ζ valid in the 'outer' region, in which capillarity is negligible, can be obtained via solution of the following equation:

$$\beta\xi\zeta + \frac{(\zeta^3 - 1)}{3}\sin\theta = 0. \tag{30}$$

This equation was obtained by integrating Eq. 28 and applying the boundary conditions $\xi \to 0$, $(\mathcal{H}, \mathcal{G}) \to (1, 0)$. Inspection of Figs. 3 and 4 reveals reasonably good agreement between the numerical predictions and the scaling exponents given by Eq. 29; the agreement with the scalings given by (26) is not as good: $(\eta + h)_{\max}$ and $x_{\max}$ appear to vary weakly with time at early times. Note that the exponents in Eq. 29 are the same as those obtained previously [1, 20] for flow down a rigid inclined plane in the absence of capillarity. We turn our attention now to the linear stability of the flow in the CF case.

4 Linear stability

We analyze the linear stability of the flow in the CF case by linearizing Eqs. 5 and 6 about the travelling-wave solutions for H and G:

$$(h, \eta)(x, y, t) = (H, G)(\xi, t) + (\psi, \phi)(\xi, t)e^{iky}, \tag{31}$$

where ψ and ϕ represent the amplitudes of the disturbances in the film thickness and wall deflection, respectively, and k is the disturbance wavenumber. We have chosen to investigate the linear stability of the CF rather than the CV case due to the existence of steady-state travelling-wave solutions in the former, which are absent in the latter case. The linearized equations governing the dynamics of the perturbations are then given by

$$B\phi_t = c\phi_\xi + \mathcal{T}\phi_{\xi\xi} - \psi_{\xi\xi} + k^2(\psi - \mathcal{T}\phi), \tag{32}$$

$$\psi_t = -\phi_t + c(\psi_\xi + \phi_\xi) + \frac{1}{3}\left[(H+G)^3\left(-\psi_{\xi\xi\xi} + k^2\psi_\xi\right) - 3(H+G)^2\left(H_{\xi\xi\xi} + \sin\theta\right)(\psi + \phi)\right]_\xi$$
$$+ \frac{1}{3}(H+G)^3 k^2\left(\psi_{\xi\xi} - k^2\psi\right). \tag{33}$$

In the absence of wall deflection effects, i.e., in the limit $\mathcal{T} \to \infty$, the linear operators in Eqs. 32 and 33 are known to be non-normal [1]. Thus, transient amplification of applied disturbances is possible which, at intermediate time-scales, may mask the behavior predicted by a standard eigenvalue analysis. In the present paper, we solve Eqs. 5, 6, 32 and 33 as an initial-value problem starting from (13) for H and G and the following initial condition for ψ and ϕ:

$$\psi(\xi, 0) = e^{(-5(\xi-10)^2)}, \quad \phi(\xi, 0) = 0, \tag{34}$$

which correspond to a perturbation applied at the leading edge of the initial front in the liquid film. Long time solutions of Eqs. 6, 5, 32 and 33 are then obtained using PDECOL over computational domains of
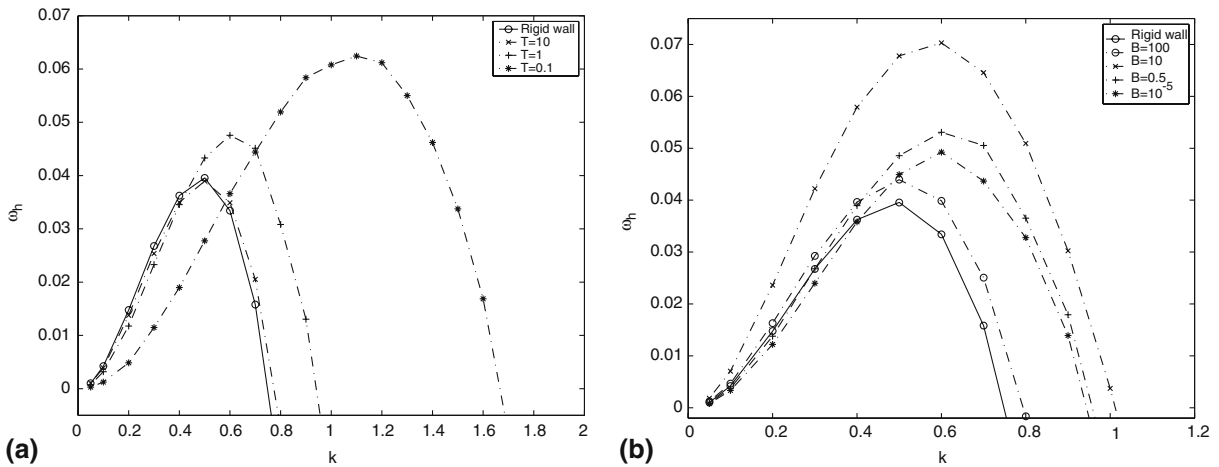
Fig. 6 The effect of varying $\mathcal{T}$ (with $B = 10^{-4}$), (**a**), and B (with $\mathcal{T} = 1$), (**b**), on the numerically generated dispersion curves

20 dimensionless units in length for $0.1 \le \mathcal{T} \le 10$ and $10^{-5} \le B \le 100$; solutions were obtained for up to $t = 10^5$. The parameters b, ϵ and θ were fixed at 0.1, 0.01 and $\pi/2$, respectively.

Measures of perturbation growth (or decay) are extracted from these long time solutions by using the following relations:

$$\omega_i =_{\lim t \to \infty} \frac{1}{2t} \log \frac{E_i(t)}{E_i(t = 0)} \quad (i = h, \eta), \tag{35}$$

where E_h and E_η correspond to perturbation 'energies' given by

$$E_h = \frac{\int_0^\infty \psi^2 \mathrm{d}\xi}{\int_0^\infty H^2 \mathrm{d}\xi}, \quad E_\eta = \frac{\int_0^\infty \phi^2 \mathrm{d}\xi}{\int_0^\infty G^2 \mathrm{d}\xi}. \tag{36}$$

Thus, the ω_i correspond to the asymptotic growth rates, which can be computed using a standard eigenvalue analysis with $(\psi, \phi) \sim \exp(\omega t)$. Using this approach we are therefore capable of capturing the dynamics at both early and late times.

In Fig. 6a we show numerically generated dispersion curves which depict the dependence of ω_h on k for different values of $\mathcal{T}$ with $B = 10^{-4}$. For every value of $\mathcal{T}$ shown, the curves exhibit bands of wavenumbers which have positive values of ω_h with clearly defined cut-off and most-dangerous 'modes'. The wavenumbers associated with these modes, are defined as k_c and k_m, respectively, the latter occurring at intermediate wavenumbers. This indicates that the system is linearly unstable to transverse perturbations of wavenumber k, which grow exponentially provided $0 \le k \le k_c$. The fastest growing mode, characterized by k_m, is the one expected to dominate the dynamics prior to the onset of nonlinearities.

From Fig. 6a it can be clearly seen that a decrease in $\mathcal{T}$ is destabilizing, giving rise to an increase in the maximal growth rate, k_m and k_c. The dispersion curve associated with $\mathcal{T} = 10$ is very similar to that generated for a rigid wall and we have ensured that this dispersion curve is identical to that previously obtained by other researchers [1, 6, 17], except that our growth rates are one-third of those found in the literature due to our choice of scaling for time. (We do not include the factor of $1/3$ in our time scales.) Interestingly, the results shown in Fig. 6 indicate that decreasing $\mathcal{T}$ exerts a stabilizing influence on the low wavenumber disturbances while destabilizing those at relatively large k values.

Next, we examine the effect of varying B on the numerically generated dispersion curves with $\mathcal{T} = 1$; this is shown in Fig. 6b. Here, we note that the effect of B on the stability characteristics is non-monotonic. A decrease in the relative significance of wall damping such that $B \sim 10^{-5}$ leads to a more unstable situation relative to the rigid-incline case, as characterized by an increase in the maximal growth rates, k_m and k_c. An increase in B to $B = 0.5$ is found to increase the maximal growth and is therefore destabilizing, although
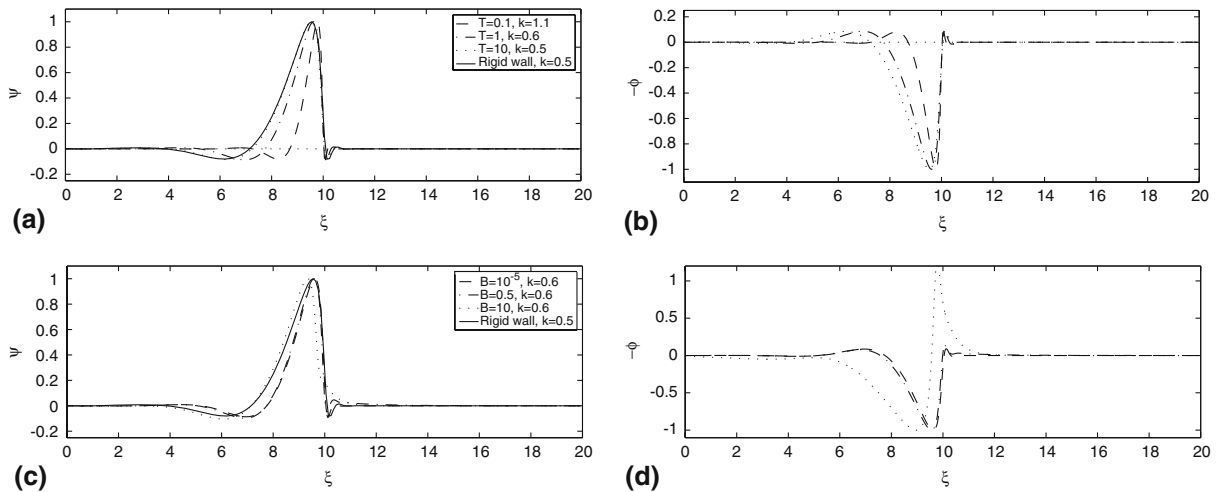
Fig. 7 Comparison of ψ and ϕ associated with the most dangerous modes in Fig. 6

k_m and k_c are left virtually unaltered. A further increase to $B = 10$ leads to even larger growth rates and an increase in k_c, while leaving k_m unaffected. If, however, B is increased to $B = 100$, then the resulting dispersion curve is very similar to that associated with the rigid-wall case. The latter result is to be expected since in the limit $B \to \infty$, one expects to recover the equations describing flow down a rigid incline.

We have also investigated the effect of varying $\mathcal{T}$ and B on the shapes of ψ and ϕ with $k = k_m$. Figure 7a, b shows that the disturbances having the largest growth rates (which are those associated with $\mathcal{T} = 0.1$ and $k = 1.1$ in this plot) are highly localized at the downward sloping part of the capillary ridge, immediately upstream of the precursor thickness region. The location of the disturbances in relation to the base-state profiles is identical to that in the rigid-wall case [1, 6, 17]. A similar examination of Fig. 7c, d, in which we plot the eigenfunctions associated with k_m for different B and $\mathcal{T} = 1$, reveals no marked differences in the shapes of ψ and ϕ for $B = 10^{-5}$ and $B = 0.5$. The profiles are more localized than those associated with the rigid-wall case. Interestingly, the ψ and ϕ profiles for $B = 10$, which is the most unstable case as shown in Fig. 6b, are not as localized. In fact, ψ in this case is very similar to that of the rigid-wall case. It is worth recalling, however, that the base state thickness profiles for $B = 10$ (Fig. 2c), exhibit more pronounced capillary ridges which may be more susceptible to transverse perturbations.

It is well known that, in the case of rigid walls, the flow is destabilized by the body force, which amplifies transverse perturbations and leads to alternating thin and thick regions that eventually form fingers [6]. The so-called Rayleigh component of the capillary pressure also provides a destabilizing, albeit smaller, contribution [6]. In order to gain insight into the roles of wall tension and damping in the instability, we form the inner product of Eq. 32 with ϕ to obtain the following equation for $E_\phi = \int_0^\infty \phi^2 \mathrm{d}\xi$:

$$\frac{1}{2}\frac{\mathrm{d}E_\phi}{\mathrm{d}t} = \frac{c}{2}\frac{\mathrm{d}E_\phi}{\mathrm{d}\xi} + \frac{1}{B}\left[\int_0^\infty \phi_\xi\psi_\xi\,\mathrm{d}\xi + k^2\int_0^\infty \psi\phi\,\mathrm{d}\xi - \mathcal{T}\int_0^\infty \phi_\xi^2\,\mathrm{d}\xi - k^2\mathcal{T}\int_0^\infty \phi^2\,\mathrm{d}\xi\right], \tag{37}$$

where the term proportional to c is due to streamwise flow in a reference frame moving with the travelling-wave. Inspection of Eq. 37 allows the identification of terms which are stabilizing or destabilizing, leading to $\mathrm{d}E_\phi/\mathrm{d}t < 0$ and $\mathrm{d}E_\phi/\mathrm{d}t > 0$, respectively.

The fourth and fifth terms on the right-hand-side of Eq. 37 that are proportional to $\mathcal{T}$, which correspond to contributions to the flow of wall tension in the streamwise and transverse directions, respectively, are both stabilizing. Hence, decreasing the value of $\mathcal{T}$ is destabilizing. The second and third terms on the right-hand side of Eq. 37, which represent capillary pressure distributions in the streamwise and transverse directions, respectively, are potentially destabilizing provided $\psi\phi > 0$ and $\psi_\xi\phi_\xi > 0$. As shown in Fig. 7 and all the cases investigated in this work, ψ and ϕ are spatially coincident and of the same sign. In fact, in

the limit $B \rightarrow 0$, it can be shown that $\phi = \psi/\mathcal{T}$. Thus, we can conclude that, in addition to the destabilizing effect of the body force, the flow is further destabilized by the coupling between the film and underlying flexible wall which arises through the capillary pressure. This happens despite the fact that decreasing $\mathcal{T}$ results in smaller capillary ridges in the film, which might be expected to lead to a more stable situation.

5 Conclusion

We have examined the flow of thin liquid films down a flexible inclined wall. Lubrication theory was used in order to derive a coupled system of evolution equations for the film thickness and wall deflection; a precursor-layer model was used to relieve the singularity at the contact line. The evolution equations are parameterized by dimensionless measures of the wall tension and damping coefficient, $\mathcal{T}$ and B, respectively, in addition to the angle of inclination from the horizontal, which was taken to be equal to $\pi/2$ throughout this work. Two flow configurations were studied: constant flux (CF), and constant volume (CV). The linear stability of the flow in the former case to transverse perturbations was also studied.

In the CF case, travelling-wave solutions were calculated. These solutions are characterized by thickened ridges in the vicinity of the contact line, and relatively flat profiles upstream, near the flow origin. The effect of $\mathcal{T}$ and B on these solutions was investigated. Our results indicate that decreasing $\mathcal{T}$ and B gives rise to larger (smaller) wall (film) deformations. In the CV case, similar observations were made regarding the effect of $\mathcal{T}$ and B on the magnitude of film and wall deformations. Although travelling waves do not exist within this configuration, self-similar scalings were determined for the film thickness and wall deflection. These scalings were found to be similar to those associated with flow down a rigid incline.

The results of the linear stability analysis revealed that the flow, which is unstable to transverse perturbations even in the rigid-wall case, is further destabilized via a decrease in $\mathcal{T}$. Our results also demonstrate the existence of an intermediate range of B values over which instability is maximized. By using a simplified 'energy' analysis, the destabilizing effect associated with wall flexibility was traced to the coupling which arises between the liquid film and underlying wall through the normal stresses. These stresses within the framework of lubrication theory comprise capillary pressures, which drive flow in the streamwise and transverse directions. Future work should examine the dynamics and stability of the flow in the nonlinear regime.

References

1. Bertozzi AL, Brenner MP (1997) Linear stability and transient growth in driven contact lines. Phys Fluids 9:530–539
2. Eres MH, Schwartz LW, Roy RV (2000) Fingering phenomena for driven coating films. Phys Fluids 12:1278–1295
3. Kataoka DE, Troian SM (1997) A theoretical study of instabilities at the advancing front of thermally driven coating films. J Colloid Interface Sci 192:350–362
4. Kondic L, Diez J (2003) Flow of thin films on patterned surfaces. Colloids Surf 214:1–11
5. Oron A, Davis SH, Bankoff SG (1997) Long-scale evolution of thin liquid films. Rev Mod Phys 69:931–980
6. Spaid MA, Homsy GM (1996) Stability of Newtonian and viscoelastic dynamic contact lines. Phys Fluids 8:460–478
7. Riley JJ, el Hak MG, Metcalfe RW (1988) Compliant coatings. Ann Rev Fluid Mech 20:393–420
8. Grotberg JB (1994) Pulomnary flow and transport phenomena. Ann Rev Fluid Mech 26:529–571
9. Berger SA, Jou L-D (2000) Flows in stenotic vessels. Ann Rev Fluid Mech 32:347–382
10. Carvalho MS, Scriven LE (1997) Deformable roll coating flows: steady state and linear perturbation analysis. J Fluid Mech 339:143–172
11. Kumaran V, Muralikrishnan R (2000) Spontaneous growth of fluctuations in the viscous flow of a fluid past a soft interface. Phys Rev Lett 84:3310–3313

12. Matar OK, Kumar S (2004) Rupture of a surfactant-covered thin liquid film on a flexible wall. SIAM J Appl Math 6:2144–2166
13. Halpern D, Grotberg JB (1992) Fluid-elastic instabilities of liquid-lined flexible tubes. J Fluid Mech 244:615–632
14. Halpern D, Grotberg JB (1993) Surfactant effects on fluid-elastic instabilities of liquid-lined flexible tubes: a model for airway closure. J Biomech Eng 115:271–277
15. Atabek HB, Lew SH (1966) Wave propagation through a viscous incompressible fluid contained in an initially stressed elastic tube. Biophys J 6:481
16. Landau LD, Lifshitz EM (1986) Theory of elasticity. Butterworth-Heineman, Dordrecht
17. Troian SM, Herbolzheimer E, Safran SA (1989) Fingering instabilities of driven spreading films. Europhys Lett 10:25–30
18. Keast P, Muir PH (1991) Algorithm 6888 EPDCOL—a more efficient PDECOL Code. ACM Trans Math Software 17:153–166
19. Edmonstone BD, Matar OK, Craster RV (2005) Coating of an inclined plane in the presence of insoluble surfactant. J Colloid Interface Sci 287:261–272
20. Huppert HE (1982) The propagation of two-dimensional and axisymmetric viscous gravity currents over a rigid horizontal surface. J Fluid Mech 121:43–58